Catalysts **2013**, *3*, 324-337; doi:10.3390/catal3010324

OPEN ACCESS

catalysts

ISSN 2073-4344

www.mdpi.com/journal/catalysts

Article

Hydroformylation of 1-Hexene over Rh/Nano-Oxide Catalysts

Maija-Liisa Kontkanen [1], Matti Tuikka [1,2], Niko M. Kinnunen [1], Sari Suvanto [1] and Matti Haukka [1,2,*]

[1] Department of Chemistry, University of Eastern Finland, P.O. Box 111, FI-80101 Joensuu, Finland; E-Mails: mlkontkanen@gmail.com (M.-L.K.); matti.tuikka@jyu.fi (M.T.); niko.kinnunen@ecocat.com (N.M.K.); sari.suvanto@uef.fi (S.S.)

[2] Department of Chemistry, University of Jyväskylä, P.O. Box 35, University of Jyväskylä, Finland

* Author to whom correspondence should be addressed; E-Mail: matti.o.haukka@jyu.fi; Tel.: +358-40-805-4666; Fax: +358-4-260-2501.

Received: 26 January 2013; in revised form: 25 February 2013 / Accepted: 6 March 2013 / Published: 21 March 2013

Abstract: The effect of nanostructured supports on the activity of Rh catalysts was studied by comparing the catalytic performance of nano- and bulk-oxide supported Rh/ZnO, Rh/SiO_2 and Rh/TiO_2 systems in 1-hexene hydroformylation. The highest activity with 100% total conversion and 96% yield of aldehydes was obtained with the Rh/nano-ZnO catalyst. The Rh/nano-ZnO catalyst was found to be more stable and active than the corresponding rhodium catalyst supported on bulk ZnO. The favorable morphology of Rh/nano-ZnO particles led to an increased metal content and an increased number of weak acid sites compared to the bulk ZnO supported catalysts. Both these factors favored the improved catalytic performance. Improvements of catalytic properties were obtained also with the nano-SiO_2 and nano-TiO_2 supports in comparison with the bulk supports. All of the catalysts were characterized by scanning electron microscope (SEM), inductively coupled plasma mass spectrometry (ICP-MS), BET, powder X-ray diffraction *(*PXRD*)* and NH_3- temperature-programmed desorption (TPD).

Keywords: nano-zinc oxide; supported catalyst; rhodium; hydroformylation of 1-hexene

---

1. Introduction

Hydroformylation is an important industrial process for the production of both linear (n) and branched (i) aldehydes and alcohols from alkenes by CO/H_2 in the presence of a transition metal catalyst [1–3]. Homogeneous rhodium catalysts have been found to be highly active and selective. The successful development of heterogeneous systems is, however, of importance, so that the drawbacks attributed to the homogenous system can be overcome, such as complications in catalyst recovery, product isolation and the high cost of rhodium [4–6]. A great number of papers have been published concerning rhodium complexes and rhodium metal supported on different supports, such as inorganic carries [2,7–11], active carbons [12,13], zeolites [14,15] or polymer [16,17].

The use of nanomaterials in catalysis systems has grown rapidly in the past few decades. Nanomaterials characteristically exhibit physical and chemical properties that differ from the bulk [18,19]. The main advantages of nanomaterials in heterogeneous catalysis arise from the increased surface area and, in the case of supported catalysts, the improved ability to disperse the active components on the support [20]. In the field of hydroformylation, the impacts of nanostructured materials on catalytic activity have been studied using transition metal nanoparticles [21–26] and nano-carbon [27–32] or nano-oxide supports [33–35]. In particular, carbon nanomaterials and both supported and non-supported transition metal nanoparticles have attracted considerable attention, due to their increased activity in hydroformylation [21–32]. Although there have been a vast number of studies concerning olefin hydroformylation catalyzed by oxide supported rhodium complexes in general [2,7–11], nano-oxide supported systems have been much less commonly studied [33–35]. Rhodium catalysts have been supported on a nanostructured Al_2O_3-ZrO_2 mixed oxide [33], modified mesoporous silica nanoparticles [34] and a dendritic nanoalumina [35]. The above examples demonstrated that the nanosupports can be used to improve the catalytic properties compared with conventional bulk supports. However, the use of nanosupports does not automatically mean better catalysts. The catalytic properties depend on factors, such as the surface area, morphology and porosity of the support, the metal content, dispersion, interactions between the metal and the support, the number and nature of Brønsted and Lewis acid sites and the number of free hydroxyl groups on the metal oxide surface. In order to achieve improvements in catalytic properties, the use of nanosupports should provide a means to affect these factors.

In the current paper, the effects of the nanostructured oxide supports with ZnO, SiO_2 and TiO_2 on Rh-catalyzed 1-hexene hydroformylation were studied. The well-known precursor, $RhCl_3 \cdot 3H_2O$ [7,29,36,37] was impregnated on nanostructured and bulk ZnO, SiO_2 and TiO_2, and their catalytic properties were investigated. The metal content, morphology, surface area and acidity of the supported rhodium catalysts were analyzed by using the inductively coupled plasma mass spectrometry (ICP-MS), scanning electron microscope (SEM), BET, powder X-ray diffraction (PXRD) and NH_3-temperature-programmed desorption (TPD) analysis. The recyclability of the most active catalysts was also investigated.

2. Results and Discussion

2.1. Catalytic Activity of Supported Catalysts

In the current work, oxide nanoparticles, especially zinc oxide, were found to be potential supporting materials for the Rh-based catalyst used in the hydroformylation of 1-hexene. The catalysis results are summarized in Table 1.

With both bulk TiO_2- and SiO_2-supported Rh catalysts, the hydroformylation activities were extremely low (entries 1 and 3), and in both cases, the activities were improved when nanosupports were used (entries 2 and 4). However, the highest activity, with 96% yield of aldehydes, was obtained with the Rh/nano-ZnO catalyst (Table 1, entry 7). The catalysis product contained mainly 1-heptanal, 2-methyl-hexanal and 2-ethyl-pentanal. The *n*/*i* ratio of 0.8 indicates that the dominant products were the branched aldehydes. In the case of the bulk Rh/ZnO, the yield of aldehydes was lower, only 76% with an *n*/*i* ratio of 1.1 (Table 1, entry 6). The dominant products were 1-heptanal, 2-methyl-hexanal and 2-ethyl-pentanal. The recyclability was also improved when the nanosupport was used. With the bulk ZnO, the activity was almost completely lost after the first run (Table 1, entry 6), due to the heavy leaching. In the case of the Rh/nano-ZnO, the activity was reduced when the catalyst was reused, but the total yield of aldehydes was still 67% now with a *n*/*i* ratio of 1.5 (Table 1, entry 8). The main reason for the higher recycling activity was that Rh/nano-ZnO was much more stable. In the first catalysis run, some leaching of Rh occurred, but in the recycle run, only minor leaching was observed. With the bulk oxide, heavy leaching continued, also during the recycle run, and practically all Rh was lost with two consecutive runs (Table 1, entries 5 and 6). This indicates that with the bulk-ZnO support, there were considerable amounts of dissolved rhodium species present, and therefore, homogeneous reactions most probably played a role in the catalysis process. With the Rh/nano-ZnO, some leaching was also observed during the first run, and it is possible that to some extent, homogeneous catalysis can occur at this stage. However, practically no leaching was observed during the first recycle run, but still, the activity remained a reasonably high 67% aldehyde yield (Table 1 entry 8). At this point, catalysis is dominated by heterogeneous reactions.

After each catalysis run, the reaction solution was analyzed by infrared (IR), ^{1}H-nuclear magnetic resonance (NMR) and mass spectrometric methods in order to identify the possible homogenous rhodium components. However, no clear indication of the formation of well-known active carbonyl components, such as $[HRh(CO)_4]$ or $[Rh_4(CO)_{12}]$, could be obtained.

As mentioned earlier, improvements in catalytic activity were observed also with all of the other tested oxides when the bulk support was changed to the corresponding nanosupport (Table 1). The rhodium catalysts on bulk TiO_2 and SiO_2 showed practically no activity, while the nanosupported TiO_2 and SiO_2 catalysts produced 34% and 77% of aldehydes with *n*/*i* ratios of 1.6 and 1.0, respectively (Table 1, entries 2 and 4). In the case of the Rh/nano-TiO_2, the catalysis product contained only 1-heptanal and 2-methyl-hexanal. The predominant products for the Rh/nano-SiO_2 were 1-heptanal, 2-methyl-hexanal and 2-ethyl-pentanal. However, with both nano-TiO_2 and nano-SiO_2, the leaching was quite considerable, and the activity was clearly lower compared to the nano-ZnO catalyst.

Table 1. Activity of the Rh/nano-oxide catalysts in hydroformylation of 1-hexene.

Entry	Catalyst/run	Rh [a] (wt%)	Rh [b] (wt%)	BET surface area (m^2/g)	Product composition (mol%)						
					Conversion%	Hexene%	Hexene isomers %	Total aldehydes%	*n*/*I* [c]	TON [d]	TOF (h^{-1})
1	Rh/TiO_2	0.55	0.45	15	-	100	-	Traces	-	-	-
2	Rh/nano-TiO_2	0.60	0.46	23	52	48	17	34	1.6	17.8	0.74
3	Rh/SiO_2	0.37	0.34	2	-	100	-	Traces	-	-	-
4	Rh/nano-SiO_2	0.47	0.22	78	100	-	23	77	1.0	43.8	1.82
5	Rh/ZnO	0.94	0.31	8	100	-	24	76	1.1	21.9	0.91
6	Rh/ZnO (the first recycle run)	0.31	-	-	10	90	3	7	0.6	6.9	0.29
7	Rh/nano-ZnO	0.83	0.67	12	100	-	4	96	0.8	24.8	1.03
8	Rh/nano-ZnO (the first recycle run)	0.67	0.66	-	98	2	31	67	1.5	31.2	1.30
9	nano-ZnO	-	-	-	-	100	-	-	-	-	-

Reaction conditions: catalyst (200 mg), toluene (5.0 mL), 1-hexene (4.0 mmol), standard cyclohexane (0.2 mL) and CO (20 bar), H_2 (20 bar), 80 °C, 3 h. [a] Metal content before a catalysis run; [b] Metal content after a catalysis run; [c] *n*/*i* = *n*-heptanal/(2-methyl-hexanal + 2-ethyl-pentanal); [d] Calculation of TON based on the total conversion.

2.2. Characterization of Supported Catalyst Systems

The reason for the different behavior of different oxides was expected to lie on the nature of the support, and therefore, the morphology and acidic properties of each oxides and catalyst systems were analyzed with SEM, BET, PXRD and NH_3-TPD.

The most important factor behind the catalytic behavior of the most active and stable catalyst, Rh/nano-ZnO, was found to be the morphology of the support particles, which permitted a higher Rh uptake and a higher number of weak acid sites. The morphology of the catalyst particles was analyzed by SEM. Figures 1A,B show SEM images of the Rh/nano-ZnO and Rh/ZnO (bulk) catalysts prior to catalysis runs. The average size and size distribution of the bulk particles were clearly larger, but both catalysts contained angular shaped particles with variable diameters. SEM images of the Rh/nano-TiO_2 and Rh/TiO_2 catalysts (Figure 1C,D) showed that the larger bulk particles again had angular spherical shapes, while the smaller nanoparticles were spherical in shape. The diameters of the bulk particle ranged approximately from 50 nm to 170 nm and the diameters of nanoparticles from 25 nm to 80 nm. Unlike the other oxides, the bulk particles of the Rh/SiO_2 had laminar structures (Figure 1F). The shapes of the Rh/nano-SiO_2 particles were quite different from the bulk material. Instead of large plates, they were formed from non-uniform aggregates of fine particles (Figure 1E).

The morphology of each catalyst system was analyzed again by SEM after hydroformylation reactions. No changes were observed with the Rh/ZnO, Rh/nano-ZnO, Rh/TiO_2 or Rh/nano-TiO_2 particles. However, the appearance of the Rh/nano-SiO_2 particles was somewhat changed. The original aggregates of fine particles had merged together, forming even larger plate-like aggregates (Figure 2).

Figure 1. Scanning electron microscope (SEM) images of (**A**) Rh/nano-ZnO; (**B**) Rh/ZnO; (**C**) Rh/nano-TiO_2; (**D**) Rh/TiO_2 ; (**E**) Rh/nano-SiO_2 and (**F**) Rh/SiO_2 particles prior to the catalysis reaction.

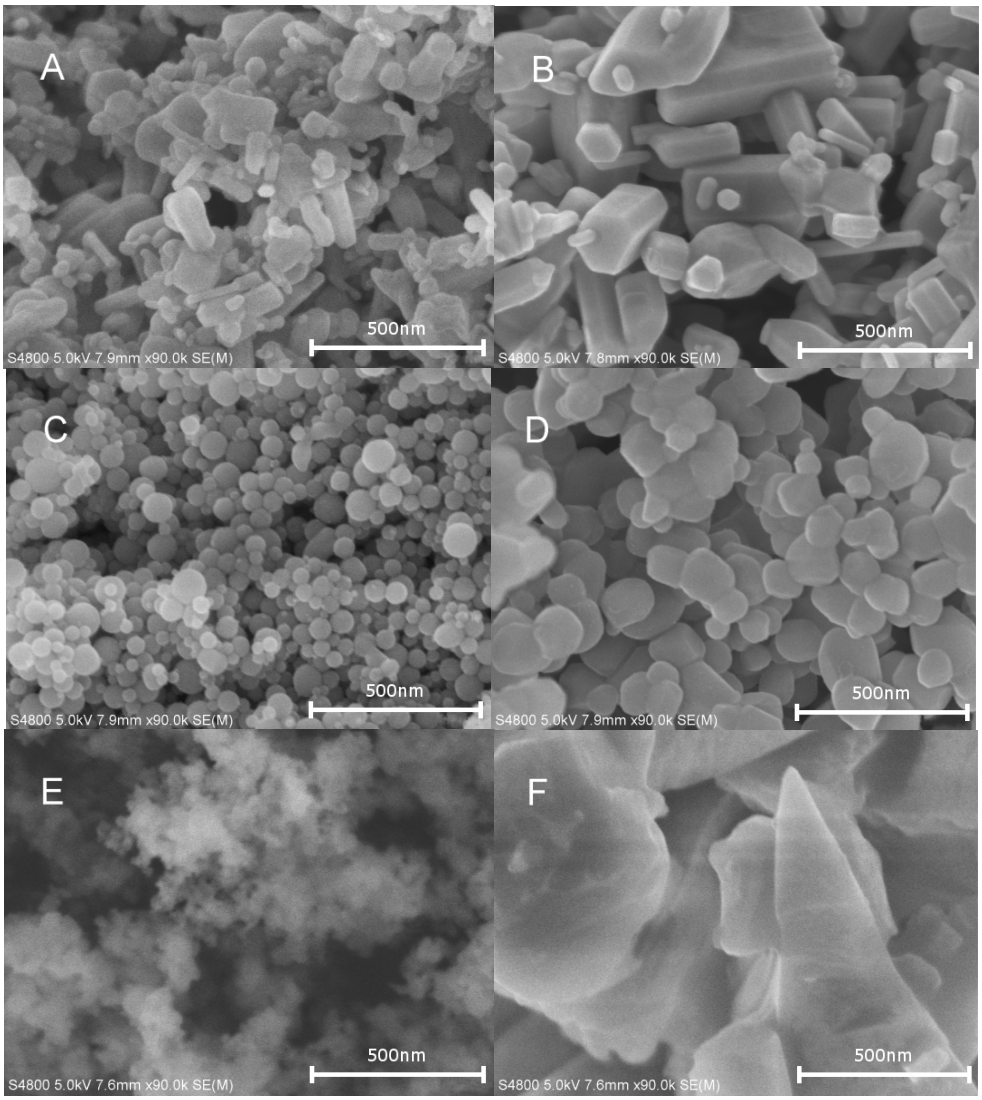

Figure 2. SEM images of the Rh/nano-SiO_2 catalyst after (**A**) impregnation and (**B**) the hydroformylation reaction.

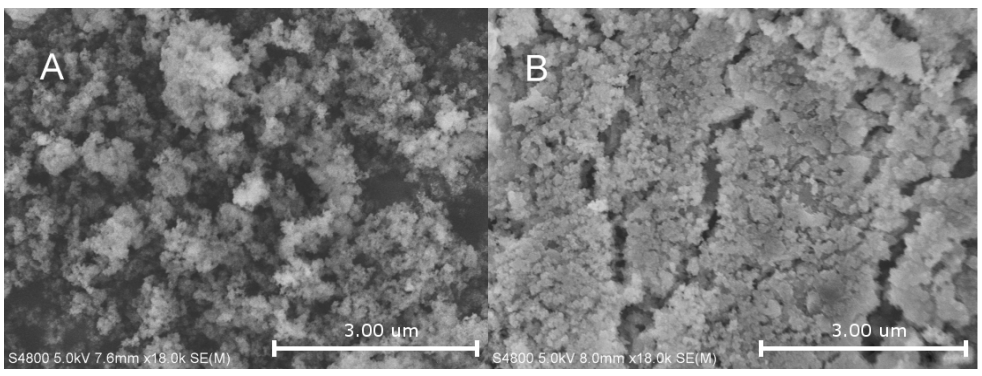

The rhodium content of all supported rhodium catalysts was determined by the ICP-MS technique, both prior to and after the hydroformylation reaction (Table 1). The rhodium content of the fresh catalysts was found to decrease in the order Rh/ZnO > Rh/nano-ZnO > Rh/nano-TiO_2 > Rh/TiO_2 > Rh/nano-SiO_2 > Rh/SiO_2. The rhodium loading was not directly correlated with the catalytic activity. The ICP-analysis gave the highest 0.94 wt% of rhodium for the fresh Rh/ZnO (bulk) catalyst before the first run, but the catalytic activity was lower when compared to the Rh/nano-ZnO (0.83 wt% of Rh). Also, the loss of Rh content was considerably higher in the case of the bulk catalyst, which indicates that the Rh/nano-ZnO catalyst is more stable than the bulk catalyst. The rhodium content of the fresh Rh/nano-SiO_2 was only 0.47 wt%, but still, the catalytic activity was at the same level with the activity of the best fresh Rh/ZnO bulk catalysts. In the case of Rh/nano-SiO_2, the initial Rh loading was only slightly higher compared to the bulk catalysts, but only the nanosupported catalyst showed any catalytic activity (Table 1 entries 3 and 4).

The dispersion of the supported rhodium on each carrier was determined qualitatively by SEM-EDS spectral images (Figures 1–6 in the Supplementary Information). The supported rhodium was uniformly dispersed on all of the supports, except the bulk Rh/SiO_2, where rhodium was clearly concentrated, forming loose aggregates, despite the relatively low metal loading (0.37 wt%). Quantitative determination of the Rh dispersion by the pulse chemisorption method using CO or H_2 as a probe gas failed, due to the low Rh loadings.

The SEM-EDS images also revealed the presence of chlorine in all of the fresh catalysts. Immediately after calcination, the rhodium was still in a cationic form, most probably as chlorides, oxychlorides or oxides. The final active phase was then obtained during the catalysis reaction when the rhodium was reduced by the syngas.

The catalysts and support materials were further analyzed by the powder X-ray diffraction method (Figures 7–12 in the Supplementary Information). Because of the low loadings and high dispersion, the Rh signals were not observed for any catalysts, except for Rh/nano-SiO_2. This indicates that rhodium forms larger crystallites on nano-SiO_2. However, according to the SEM images, the overall distribution of Rh is still uniform throughout the support material. The crystallite sizes of the supporting oxides, determined by PXRD, were close to the particle sizes observed with the SEM. For the bulk SiO_2, the average crystallite size was 130 nm, for the bulk TiO_2 and ZnO, 85 nm. The crystallite sizes of the nano-TiO_2 were TiO_2 30 nm and the nano-ZnO, 68 nm. Due to the weak signals, a reliable crystallite size could not be determined for the nano-SiO_2. However, the crystallite size was approximated to be about 30 nm.

The BET surface areas of the supported rhodium catalysts are summarized in Table 1. No direct correlation could be found between the BET surface areas and the activities of the nano- or bulk-oxide catalysts. In the case of the Rh/nano-SiO_2 and Rh/nano-TiO_2 catalysts, the higher activity of the silica system could be explained by its higher BET surface area. However, the Rh/nano-ZnO had the smallest surface among the nano-supports, but it still showed the highest catalytic activity. This is a clear indication that factors other than surface area must also have an impact on the catalytic behavior.

The number of Brønsted and Lewis acid sites on the surface of all of the metal oxides is known to be an important factor in catalytic activity [38–44]. Brønsted and Lewis sites are often simultaneously present on the same surfaces, where they form densely populated patches [38]. The analyses of the acidity of all of the supported catalysts and of the pure ZnO and SiO_2 nanosupports were carried out

using the NH_3-TPD technique. The analysis of the Rh/nano-oxide and bulk oxide catalysts indicated that two types of NH_3 adsorption sites were present, *i.e.*, weak and strong acid sites (Table 2 and Figure 3).

Table 2. Acidic surface areas, NH_3 consumptions and NH_3 consumption per BET surface areas of Rh based catalysts.

Entry	Catalyst	Acidic areas (%) [a]		NH_3 consumption (ml/$g_{Cat.}$)			NH_3 consumption per BET surface area (mL/m^2)		
		Weak [b]	Strong [c]	Weak [d]	Strong [d]	Total [e]	Weak [f]	Strong [f]	Total [f]
1	Rh/nano-ZnO	80.3	19.7	2.09	0.51	2.61	0.174	0.043	0.217
2	Rh/ZnO	50.3	49.7	0.66	0.65	1.31	0.082	0.081	0.164
3	Rh/nano-TiO_2	55.7	44.3	1.48	1.17	2.65	0.064	0.051	0.115
4	Rh/TiO_2	47.3	52.7	0.31	0.35	0.66	0.021	0.023	0.044
5	Rh/nano-SiO_2	94.2	5.8	4.84	0.30	5.14	0.062	0.004	0.066
6	Rh/SiO_2	0	100.0	0	0.33	0.33	0	0.164	0.164

[a] Surface areas were evaluated by convolution using Origin 7 software [45]. [b] Weak acid sites appear from 40 °C up to 230 °C. [c] Strong acid sites appear between 230 °C and 400 °C. [d] The number of acid sites was calculated using acidic areas and total NH_3 consumptions. [e] NH_3 consumptions were obtained by GRAMS/32 software [46]. [f] The acidities obtained were divided by the BET surface area (see Table 1).

Desorption from the weak acid site of the nano-supported catalysts produced a broad desorption signal, ranging from 40 °C to 250 °C (Figure 3). Desorption from the strong acid sites led to a narrower, but tailing signal between 230 °C and 400 °C. The proportion of weak and strong sites relative to the total number of acidic sites was examined by means of the convolution integral (Table 2 and Figures 13 and14 in the Supplementary Information). As can be seen in Figure 3 and Table 2, the Rh/nano-SiO_2 has the highest relative amount (94.2%) of weak acid sites. On the other hand, the bulk SiO_2 had only strong acid sites. In all cases, the nano-supported catalysts had more weak acid sites than the corresponding bulk catalysts. When the consumption of NH_3 per BET surface area is taken into account, the number of weak acid sites decreased in the order Rh/nano-ZnO > Rh/ZnO > Rh/nano-TiO_2 > Rh/nano-SiO_2 > Rh/TiO_2 > Rh/SiO_2 (Table 2). Except for the Rh/nano-SiO_2, the number of weak acid sites correlates directly with the catalytic activity. The Rh/nano-ZnO has the highest number of weak acid sites (0.174 mL/m^2) and the highest catalytic activity. The Rh/nano-SiO_2 displays the same catalytic activity as the bulk Rh/ZnO, but the number of weak acid sites (NH_3 consumption/BET surface area) is lower than in the case of Rh/ZnO (Table 2, entries 2 and 5). The main difference between the Rh/nano-SiO_2 and bulk Rh/ZnO catalysts lies in the number of strong acid sites. The Rh/nano-SiO_2 lacks the strong acid sites almost completely, which indicates that a low number of strong acid sites also favor the catalytic performance.

The effect of solvent, calcination and rhodium loading on the surface acidity was investigated by using the most favorable support, *i.e.*, nano-ZnO (Figure 4). Treatment of the pure nano-ZnO with ethanol and then of the subsequent calcination had no impact on the acidity. Clear signals were observed only with the rhodium containing Rh/nano-ZnO. The results suggest that the acidity arises from the supported rhodium and is not influenced by the solvent. The acidity of the nano-TiO_2 system was also caused mainly by the supported rhodium. With respect to the nanosupports, the nano-TiO_2 had the greatest basicity, due to the weaker electronegativity of the metal ions [9,47]. The SEM-EDS

images revealed the presence of chlorine in all of the fresh catalysts (Figures 1–6 in the Supplementary Information). Therefore, acidity can also be affected by the surface chloride. The calcination at 400 °C may not be enough to release all chloride from the catalyst [48].

Figure 3. NH_3-temperature-programmed desorption (TPD) curves of the (a) Rh/nano-TiO_2; (b) Rh/nano-ZnO and (c) Rh/nano-SiO_2 catalysts.

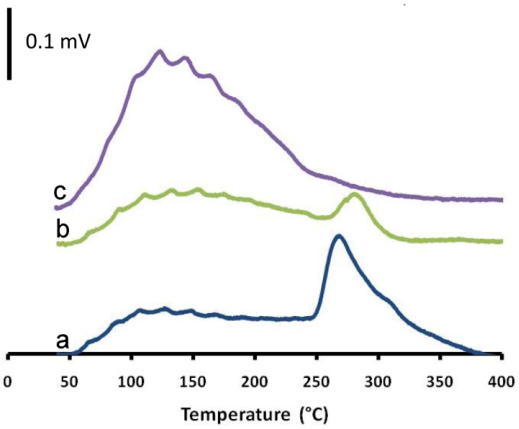

Figure 4. NH_3-TPD curves of (a) nano-ZnO, (b) solvent treated and calcinated nano-ZnO and (c) Rh/nano-ZnO.

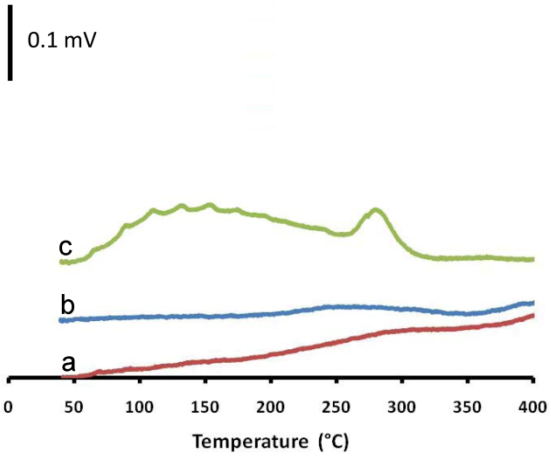

Figure 5. NH_3-TPD curves of (a) nano-SiO_2 and (b) Rh/nano-SiO_2.

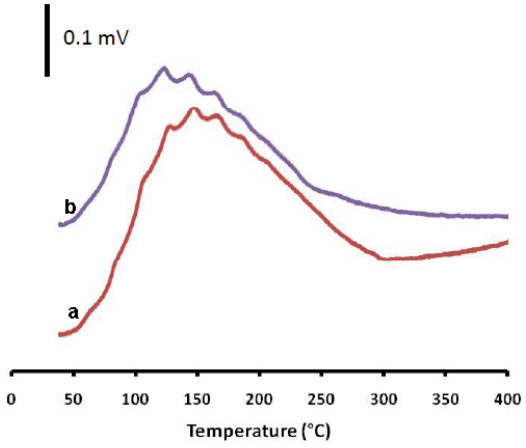

In the case of nano-SiO_2, the acidity was caused mainly by the support itself (Figure 5) and in the case of Rh/nano-SiO_2, possibly also by surface chloride [48]. However, rhodium loading changed the acidic properties only slightly. Such results indicate clearly the impact of supports of a different nature. Due to the different surface properties, one can also expect that the interactions between the support and the active component are different in the cases of Rh/nano-SiO_2 and Rh/nano-ZnO.

2.3. The Impact of Morphology on the Catalytic Activity

As a result of the favorable morphology of the zinc oxide nanoparticles, high initial metal loading and the highest number of weak acid sites were found in the Rh/nano-ZnO catalyst, favoring catalytic activity. Because of this, the Rh/nano-ZnO catalyst is expected to be able to coordinate 1-hexene and CO more effectively, thus improving the catalytic activity. On the other hand, the Rh/nano-ZnO catalyst was also clearly the most stable system, with only minor metal leaching in recycle runs. In our supported Rh systems, it is likely that the impregnated Rh^{3+} is reduced by the syngas, subsequent to which the reaction follows a route similar to that suggested by Zhou *et al.* and Rosales *et al.* for the heterogeneous olefin hydroformylation [34,49]. The hydroxyl groups on metal oxide surfaces are also known to have an impact on the catalytic activity [50–52], but their role was not studied in detail in the current work.

One of the reasons why the morphology of the bulk and nano-ZnO particles plays such an important role is most probably their morphological stability in hydrothermal treatments, drying and heating. Hydrothermal treatments of oxides may change the morphology of primary particles, resulting in changes, for example, in the specific surface area, the adsorption capacity and the adsorption-desorption of water [53–55]. As can be seen from the powder X-ray diffractograms in the case of the three most active catalyst systems (Figures 7–12 in the Supplementary Information), the crystallinity of the nano- and bulk-ZnO [56,57] did not change during the hydrothermal treatments. Furthermore, the crystallinity of ZnO improves the adsorption capacity by making more sites available for Rh adsorption. When the consumption of NH_3 per BET surface area is taken into account, the morphology of nano- and bulk-ZnO also seems to favor the higher number of the weak acid sites.

3. Experimental Section

The supported rhodium catalysts with a calculated 1 wt% metal loading were prepared by impregnation from ethanol (99.5 wt%, Altia corporation, Helsinki, Finland) $RhCl_3 \cdot 3H_2O$ (A Johnson Matthey Company, London, UK) solution. The supports used were the inorganic bulk and nanostructured oxides, SiO_2, TiO_2 and ZnO. Prior to impregnation, the silica supports, SiO_2 (Fluka/Sigma-Aldrich, St. Louis, MO, USA) and nano-SiO_2 (10–20 nm, Aldrich 99.5%, St. Louis, MO, USA) were dehydrated at 400 °C for 5 h and TiO_2 (Riedel-de-Haën 99%, Seelze, Germany), nano-TiO_2 (< 100 nm, Aldrich > 97%, St. Louis, MO, USA), ZnO (Fluka > 99%, St. Louis, MO, USA) and nano-ZnO (<100 nm, Sigma-Aldrich 99.5%, St. Louis, MO, USA) were dehydrated at 200 °C for 5 h. The $RhCl_3 \cdot 3H_2O$ (0.0512 g) was dissolved in ethanol (20 mL), and the oxide support (2.0 g) was added to the mixture. The suspension was mixed overnight. After solvent evaporation, the resulting samples were calcinated at 400 °C under high vacuum for 2 h.

Scanning electron microscope (SEM) images were recorded using a Hitachi S4800 scanning electron microscope equipped with an EDS unit (Thermo Electron, Tokyo, Japan). The rhodium content of the supported catalysts was determined by an inductively coupled plasma mass spectroscopy (ICP-MS) technique. The BET surface areas of the supported catalysts were measured using a Micrometrics ASAP 2010 (Norcross, GA, USA). A sample was pretreated in vacuum at 250 °C for 2 h, and the measurement was carried out at the temperature of liquid nitrogen. The PXRD measurements were carried out with a Bruker-AXS D8 Advance device using Cu Kα as the radiation source. The diffraction pattern was collected between 4° and 80° at 2θ scale with a step size of 0.05° and measuring of 3 s/step or 015 s/step. The crystallite sizes were evaluated from the diffraction data with TOPAS 4.2 software [58]. Ammonia temperature-programmed desorption (NH_3-TPD) of the samples was carried out using a Micrometritics AutoChem 2910 instrument equipped with a thermal conductivity detector. A sample (100 mg) was pretreated at 400 °C under helium flow (30 mL/min) for 2 h, and after cooling, 10% NH_3/He mixed gas at 40 °C was fed at a flow rate of 30 mL/min for 1 h. Physically adsorbed NH_3 was removed by flushing the sample with a helium flow of 30 mL/min for 1 h. Desorption of ammonia was measured by heating between 40 °C and 400 °C at a rate of 20 °C/min with a helium flow of 020 mL/min. Integration of the peaks was carried out using the GRAMS/32 program [46].

The hydroformylation reactions were performed in a 100-mL high-pressure autoclave (Berghof, Eningen, Germany) equipped with a 75-mL Teflon liner. In a typical reaction, the toluene solvent (Riedel-de-Haën 99.7%, Seelze, Germany) (5.0 mL), the olefin 1-hexene (Aldrich 99+%, St. Louis, MO, USA) (0.5 mL), the internal standard cyclohexane (Sigma-Aldrich 99+%, St. Louis, MO, USA) (0.2 mL) and the supported rhodium catalyst (0.200 g) were introduced into the autoclave, which was then pressurized with CO (20 bar) and H_2 (20 bar) (AGA 99.99%, Lidingö, Sweden). The reaction temperature was 80 °C and the reaction time was 3 h. After the reaction, the autoclave was cooled in liquid nitrogen and brought to atmospheric pressure. Gas chromatographic analysis of the product solutions was carried out using a Hewlett-Packard 5890 series II chromatograph equipped with a Varian WCOT fused silica column (50m × 0.53mm).

4. Conclusions

The nanostructured carriers, ZnO, SiO_2 and TiO_2, were found to improve the catalytic performance of the supported Rh catalyst compared with the corresponding bulk oxides. The highest activities in 1-hexene hydroformylation were obtained with the Rh/nano-ZnO catalyst, giving 96% of aldehydes. The angular spherical morphology of catalyst particles with a high rhodium content and a higher number of weak acid sites favored catalytic activity of the catalysts. On the other hand, a larger number of strong acid sites had a tendency to reduce activity. The use of a nanostructured support also reduced the leaching of the Rh and improved the stability and recyclability of the catalysts. In the case of the most active Rh/nano-ZnO, some loss of Rh occurred during the first catalysis run, but no severe loss of Rh content was observed during the subsequent run.

Acknowledgements

Financial support provided by the Academy of Finland (project No. 115985) is gratefully acknowledged (Maija-Liisa Kontkanen, Matti Haukka). The authors also wish to thank the Institute for Environmental Research at the University of Jyväskylä for the ICP-MS analysis.

References

1. Frohning, C.D.; Kohlpaintner, C.W.; Bohnen, H.W. In *Applied Homogeneous Catalysts with Organometallic Compounds*, 2nd ed.; Cornils, B., Herrmann, W.A., Eds.; Wiley-VCH: Weinheim, Germany, 2002; Volume 1, pp. 31–103.
2. Likholobov, V.A.; Moroz, B.L. In *Handbook of Heterogeneous Catalysis*, 2nd ed.; Ertl, G., Knözinger, H., Schüth, F., Weitkamp, J., Eds.; Wiley-VCH Verlag GmbH & Co: Weinheim, Germany, 2008; Volume 5, pp. 2231–2241.
3. Srivastava, V.K.; Sharma, S.K.; Shukla, R.S.; Subrahmanyam, N.; Jasra, R.V. Kinetic Studies on the Hydroformylation of 1-Hexene Using RhCl(AsPh3)3 as a Catalyst. *Ind. Eng. Chem. Res.* **2005**, *44*, 1764–1771.
4. Zhang, Y.; Nagasaka, K.; Qui, X.; Tsubaki, N. Low-pressure hydroformylation of 1-hexene over active carbon-supported noble metal catalysts. *Appl. Catal. A* **2004**, *276*, 103–111.
5. Qiu, X.; Tsubaki, N.; Sun, S.; Fujimoto, K. Influence of noble metals on the performance of Co/SiO_2 catalyst for 1-hexene hydroformylation. *Fuel* **2002**, *81*, 1625–1630.
6. Tadd, A.R.; Marteel, A.; Mason, M.R.; Davies, J.A.; Abraham, M.A. Hydroformylation of 1-Hexene in Supercritical Carbon Dioxide Using a Heterogeneous Rhodium Catalyst. 2. Evaluation of Reaction Kinetics. *Ind. Eng. Chem. Res.* **2002**, *41*, 4514–4522.
7. Han, D.; Li, X.; Zhang, H.; Liu, Z.; Li, J.; Li, C. Heterogeneous asymmetric hydroformylation of olefins on chirally modified Rh/SiO_2 catalysts. *J. Catal.* **2006**, *243*, 318–325.
8. Balacos, M.W.; Chuang, S.S.C. Transient Response of Propionaldehyde Formation During $CO/H_2/C_2H_4$ Reaction on Rh/SiO_2. *J. Catal.* **1995**, *151*, 253–265.
9. Bando, K.K.; Asakura, K., Arakawa, H.; Isobe, K.; Iwasawa, Y. Surface Structures and Catalytic Hydroformylation Activities of Rh Dimers Attached on Various Inorganic Oxide Supports. *J. Phys. Chem.* **1996**, *100*, 13636–13645.
10. Nandi, M.; Mondal, P.; Islam, M.; Bhaumik, A. Highly Efficient Hydroformylation of 1-Hexene over an *ortho*-Metallated Rhodium(I) Complex Anchored on a 2D-Hexagonal Mesoporous Material. *Eur. J. Inorg. Chem.* **2011**, *2*, 221–227.
11. Ichikawa, M. Catalytic hydroformylation of olefins over the rhodium, bimetallic RhCo, and cobalt carbonyl clusters supported with some metal oxides. *J. Catal* **1979**, *59*, 67–78.
12. Kainulainen, T.A.; Niemelä, M.K.; Krause, A.O.I. Hydroformylation of 1-hexene on Rh/C and Co/SiO_2, catalysts. *J. Mol. Cat. A* **1997**, *122*, 39–49.
13. Li, B.; Li, X.; Asami, K.; Fujimoto, K. Low-Pressure Hydroformylation of Middle Olefins over Co and Rh Supported on Active Carbon Catalysts. *Energy Fuels* **2003**, *17*, 810–816.
14. Mukhopadhyay, K.; Chaudhari, R.V. Heterogenized $HRh(CO)(PPh_3)_3$ on zeolite Y using phosphotungstic acid as tethering agent: a novel hydroformylation catalyst. *J. Catal.* **2003**, *213*, 73–77.

15. Takahashi, N.; Miura, K.; Fukui, H. Reaction of rhodium species with carbon monoxide on freshly prepared Rh-Y zeolite and rhodium trichloride/silica catalysts revealed by the carbon-13 NMR technique. *J. Phys. Chem.* **1986**, *90*, 2797–2800.
16. Shibahara, F.; Nozaki, K.; Matsuo, T.; Hiyama, T. Asymmetric Hydroformylation with Highly Crosslinked Polystyrene-Supported (*R*,*S*)-BINAPHOS–Rh(I) Complexes: The Effect of Immobilization Positions. *Bioorg. Med. Chem. Lett.* **2002**, *12*, 1825–1827.
17. Nozaki, K.; Itoi, Y.; Shibahara,F.; Shirakawa, E.; Ohta, T.; Takaya, H.; Hiyama, T. Asymmetric Hydroformylation of Olefins in a Highly Cross-Linked Polymer Matrix. *J. Am. Chem. Soc.* **1998**, *120*, 4051–4052.
18. Ozin, G.A.; Arsenault, A.C. *Nanochemistry a Chemical Approach to Nanomaterials*; RSC Publishing: London, China, 2005; p. 5.
19. Rao, C.N.R.; Müller, A.; Cheetham A.K. In *The Chemistry of Nanomaterials Synthesis, Properties and Applications*; Rao, C.N.R., Müller, A., Cheetham, A.K., Eds; VCH: Weinheim, Germany, 2004; Volume 1, pp. 1–2.
20. Park, K.H.; Ku, I.; Kim, H.J.; Son, S.U. NHC-Based Submicroplatforms for Anchoring Transition Metals. *Chem. Mater.* **2008**, *20*, 1673–1675.
21. Tuchbreiter, L.; Mecking, S. Hydroformylation with Dendritic-Polymer-Stabilized Rhodium Colloids as Catalyst Precursors. *Macromol. Chem. Phys.* **2007**, *208*, 1688–1693.
22. Han, M.; Liu, H. Reaction conducted under rather severe conditions for a colloidal catalyst - hydroformylation of propylene catalyzed by polymer-protected rhodium colloids. *Macromol. Symp.* **1996**, *105*, 179–183.
23. Bruss, A.J.; Gelesky, M.A.; Machado, G.; Dupont, J. Rh(0) nanoparticles as catalyst precursors for the solventless hydroformylation of olefins. *J. Mol. Catal. A* **2006**, *252*, 212–218.
24. Cai, Z.; Wang, H.; Xiao, C.; Zhong, M.; Ma, D.; Kou, Y. Hydroformylation of 1-hexene over ultrafine cobalt nanoparticle catalysts. *J. Mol. Catal. A* **2010**, *330*, 94–98.
25. Han, D.; Li, X.; Zhang, H.; Liu, Z.; Hu, G.; Li, C. Asymmetric hydroformylation of olefins catalyzed by rhodium nanoparticles chirally stabilized with (*R*)-BINAP ligand. *J. Mol. Catal. A* **2008**, *283*, 15–22.
26. Kim, J.Y.; Park, J.H.; Jung, O.-S.; Chung, Y.K.; Park, K.H. Heterogenized Catalysts Containing Cobalt-Rhodium Heterobimetallic Nanoparticles for Olefin Hydroformulation. *Catal. Lett.* **2009**, *128*, 483–486.
27. Oresmaa, L.; Moreno, M.A.; Jakonen, M.; Suvanto, S.; Haukka, M. Catalytic activity of linear chain ruthenium carbonyl polymer $[Ru(CO)_4]_n$ in 1-hexene hydroformylation. *Appl. Catal. A* **2009**, *353*, 113–116.
28. Giordano, R.; Serp, P.; Kalck, P.; Kihn, Y.; Schreiber, J.; Marhic, C.; Duvail, J.-L. Preparation of Rhodium Catalysts Supported on Carbon Nanotubes by a Surface Mediated Organometallic Reaction. *Eur. J. Inorg. Chem.* **2003**, *4*,610–617.
29. Zhang, Y.; Zhang, H.-B.; Lin, G.-D.; Chen, P.; Yuan, Y.-Z.; Tsai, K.R. Preparation, characterization and catalytic hydroformylation properties of carbon nanotubes-supported Rh–phosphine catalyst. *Appl. Catal. A* **1999**, *187*, 213–224.

30. Qiu, J.; Zhang, H.; Liang, C.; Li, J.; Zhao, Z. Co/CNF Catalysts Tailored by Controlling the Deposition of Metal Colloids onto CNFs: Preparation and Catalytic Properties. *Chem. Eur. J.* **2006**, *12*, 2147–2151.
31. Serp, P.; Cossias, M.; Kalck, P. Carbon nanotubes and nanofibers in catalysis. *Appl. Catal. A* **2003**, *253*, 337–358.
32. Gao, R.; Tan, C.D.; Baker, R.T.K. Ethylene hydroformylation on graphite nanofiber supported rhodium catalysts. *Catal. Today* **2001**, *65*, 19–29.
33. Wryszcz, J.; Zawadzki, M.; Treciak, A.M.; Tylus, W.; Ziolkokowski, J.J. Catalytic activity of rhodium complexes supported on $Al._2O_3$-ZrO_2 in isomerization and hydroformylation of 1-hexene.. *Catal. Lett.* **2004**, *93*, 85–92.
34. Zhou, W.; He, D. Anchoring $RhCl(CO)(PPh_3)$(2) to -$PrPPh_2$ Modified MCM-41 as Effective Catalyst for 1-Octene Hydroformulation. *Catal. Lett.* **2009**, *127*, 437–443.
35. Li, P.; Thitsartan, W.; Kawi, S. Highly Active and Selective Nanoalumina-Supported Wilkinson's Catalysts for Hydroformylation of Styrene. *Ing. Eng. Chem. Res.* **2009**, *48*, 1824–1830.
36. Zimowska, M.; Wagner, J.B.; Dziedzic, J.; Camra, J.; Borzęcka-Prokop, B.; Najbar, M. Some aspects of metal-support strong interactions in Rh/Al_2O_3 catalyst under oxidising and reducing conditions. *Chem. Phys. Lett.* **2006**, *417*, 137–142.
37. Vishwanathan, V.; Narayanan, S. Evidence for strong metal-support interaction (SMSI) in Rh/TiO_2 system. *Catal. Lett.* **1993**, *21*, 183–189.
38. Lónyi, F.; Valyon, J. On the interpretation of the NH_3-TPD patterns of H-ZSM-5 and H-Mordenite. *Micropor. Mesopor. Mater.* **2001**, *47*, 293–301.
39. Zecchina, A.; Lamberti, C.; Bordiga S. Surface acidity and basicity: General concepts. *Catal. Today* **1998**, *41*, 169–177.
40. Busca, G. Spectroscopic characterization of the acid properties of metal oxide catalysts. *Catal. Today* **1998**, *41*, 191–206.
41. Morrow, B.A.; Cody, I.A. Infrared studies of reactions on oxide surfaces. 5. Lewis acid sites on dehydroxylated silica and Infrared studies of reactions on oxide surfaces. 6. Active sites on dehydroxylated silica for the chemisorption of ammonia and water. *J. Phys. Chem.* **1976**, *80*, 1995–2004.
42. Wang, X.; Sonström, P.; Arndt, D.; Stöver, J.; Zielasek, V.; Borchert, H., Thiel, K.; Al-Shamery, K.; Bäumer, M. Heterogeneous catalysis with supported platinum colloids: A systematic study of the interplay between support and functional ligands. *J. Catal.* **2011**, *278*, 143–152.
43. Ordomsky, V.V.; Sushkevich, V.L.; Ivanova, I.I. Study of acetaldehyde condensation chemistry over magnesia and zirconia supported on silica. *J. Mol. Catal. A* **2010**, *333*, 85–93.
44. Busca, G. *Metal Oxide Catalysis;* Jackson, S.D., Justin, S.J., Eds.; The Use of Infrared Spectroscopic Methods in the Field of Heterogeneous Catalysis by Metal Oxides. **2009**, *1*, 95–175.
45. *Origin 7 SR2 Software*, version 7.0383; OriginLab: Northampton, MA, USA , 2002.
46. *GRAMS/32*, version 4.0; Galactic Industries Corporation: Salem, NH, USA.
47. Zumdahl, S.S. *Chemical Principles*, 3rd ed.; Houghton Mifflin Company: Boston, MA, USA, 1998; p. 572.

48. Newkirk, A.E.; McKee, D.W. Thermal decomposition of rhodium, iridium, and ruthenium chlorides. *J. Catal.* **1968**, *11*, 370–377.
49. Rosales, M.; Durán, J.A.; Gonález, Á.; Pacheco, I.; Sánchez-Delgado, R.A. Kinetics and mechanisms of homogeneous catalytic reactions. Part 7. Hydroformylation of 1-hexene catalyzed by cationic complexes of rhodium and iridium containing PPh_3. *J. Mol. Catal.* **2007**, *270*, 250–256.
50. Parfitt, G.D. Surface chemistry of oxides. *Pure Appl. Chem.* **1976**, *48*, 415–418.
51. Gun'ko, V.M. Competitive adsorption. *Theor. Experim. Chem.* **2007**, *43*, 139–183.
52. Noei, H.; Qui, H.; Wang, Y.; Löffler, E.; Wöll, C.; Muhler, M. The identification of hydroxyl groups on ZnO nanoparticles by infrared spectroscopy. *Phys. Chem. Chem. Phys.* **2008**, *10*, 7092–7097.
53. Gun'ko, V.M.; Leboda, R.; Skubiszewska-Zięba, J. Heating effects on morphological and textural characteristics of individual and composite nanooxides. *Adsorption* **2009**, *15*, 89–98.
54. Gun'ko, V.M.; Zarko, V.I.; Turov, V.V.; Oranska, O.I.; Goncharuk, E.V.; Nychiporuk, Y.M.; Pakhlov, E.M.; Yurchenko, G.R.; Leboda, R.; Skubiszewska-Zięba, J.; *et al.* Morphological and structural features of individual and composite nanooxides with alumina, silica, and titania in powders and aqueous suspensions. *Powder Technol.* **2009**, *195*, 245–258.
55. Gun'ko, V.M.; Yurchenko, G.R.; Turov, V.V.; Goncharuk, E.V.; Zarko, V.I.; Zabuga, A.G.; Matkovsky, A.K.; Oranska, O.I.; Leboda, R.; Skubiszewska-Zięba, J.; *et al.* Adsorption of polar and nonpolar compounds onto complex nanooxides with silica, alumina, and titania. *J. Colloid Interface Sci.* **2010**, *348*, 546–558.
56. Karin, A.M.; Conant, T.; Datye, A.K. Controlling ZnO morphology for improved methanol steam reforming reactivity. *Phys. Chem. Chem. Phys.* **2008**, *10*, 5584–5590.
57. Li, G.R.; Hu, T.; Pan, G.L.; Yan, T.Y.; Gao, X.P.; Zhu, H.Y. Morphology−Function Relationship of ZnO: Polar Planes, Oxygen Vacancies, and Activity. *J. Phys. Chem. C* **2008**, *112*, 11859–11864.
58. *TOPAS V4.2: General Profile Analysis Software for Powder Diffraction Data*; Bruker AXS: Karsruhe, Germany, 2008.